npj | computational materials

Article

Published in partnership with the Shanghai Institute of Ceramics of the Chinese Academy of Sciences

https://doi.org/10.1038/s41524-024-01246-1

Addressing the effects of gas adsorption on monolayers beyond charge population analysis: the case of WS_2

Michele Giovanni Bianchi ✉, Francesca Risplendi, Michele Re Fiorentin [2] & Giancarlo Cicero [2]

The optoelectronic properties of two-dimensional (2D) materials can be significantly influenced by charge transfer resulting from surface molecular adsorption. One noteworthy example is observed in WS_2 monolayers, where the behavior undergoes an anomalous change when exposed to air, primarily due to the adsorption of oxygen molecules. While the acceptor nature of O_2 is widely acknowledged as the underlying cause, the precise electron transfer mechanism remains in need of a comprehensive explanation at the atomistic level. Going beyond conventional charge population analysis, we develop an approach describing the process of molecular adsorption and surface charge transfer that relies on the formalism commonly adopted for charged defects in semiconductors. This method clearly identifies two key factors contributing to electron transfer upon O_2 physisorption: the presence of sulphur vacancies and the intrinsic *n*-type nature of WS_2. This approach provides an effective and general scheme to characterize the surface charge transfer in 2D materials exposed to a gas atmosphere.

In the field of quantum information technologies, precision metrology, and imaging applications, 2D materials with semiconducting properties have emerged as a new class of optical sources offering the potential for high photon yield, excellent spectral purity, and controllable emission of coherent photons[1–5]. Among them, monolayers (MLs) of WS_2, a transition-metal dichalcogenide (TMD), stand out as particularly appealing, thanks to their semiconducting character with a direct band gap in the visible range (≈ 2 eV)[6]. Furthermore, WS_2 MLs can be synthesized in large flakes using common growth techniques, such as molecular beam epitaxy (MBE) or, more frequently, chemical vapor deposition (CVD)[7–9].

WS_2 MLs generally display an *n*-type character[10] and, due to the large surface-to-volume ratio, their optoelectronic properties are strongly affected by the surrounding environment, undergoing significant modifications upon exposure to the ambient atmosphere[11–13]. Among the different gases in air, molecular oxygen has been identified as having the largest impact on WS_2 properties[14,15], decreasing the material conductivity[16–18] and altering the photoluminescence (PL) emission spectra[19–21]. Notably, the PL yield of WS_2 MLs experiences a significant enhancement when measurements are conducted in air as opposed to a vacuum environment[14,22,23]. This phenomenon has been attributed to the electron withdrawal from the material by adsorbed O_2 molecules. As a result, the free electron density in the intrinsically *n*-type samples is reduced, promoting the formation and subsequent radiative recombination of neutral excitons, while suppressing the intensity of the negative trion peak[14,20,21].

Several experiments have investigated the chemisorption of O_2 on WS_2 MLs[22–24]. However, being an energy-activated process, the impact of chemisorption on the PL becomes significant only at high laser power density and/or long irradiation time. Consequently, the primary contribution to the PL enhancement in air has been attributed to the spontaneous O_2 physisorption on the basal plane of the material[20,25]. It is commonly supposed that O_2 withdraws electrons when physisorbed on the pristine ML. The majority of theoretical analyses of molecular adsorption on 2D materials are performed considering pristine surfaces[16,25–27]. However, it is well-established that synthesized 2D materials exhibit a diverse array of defects. Extensive characterization efforts have been undertaken to assess the impact of these defects on the electronic[28–32] and catalytic properties[33–35] of WS_2. The enhanced reactivity of defect sites towards a wide range of chemical species, such as H_2, O_2, CO_2, and NO_2[35] clearly proves the importance of defects in the adsorption process. Consequently, when describing O_2 adsorption on WS_2, it is crucial to include in the analysis also common defects, such as sulfur vacancies (V_S) [36].

Although the role of O_2 adsorption in the observed variations of the optical response of WS_2 has been established, the most effective adsorption site and the proposed electron transfer mechanism at the core of this

Department of Applied Science and Technology, Politecnico di Torino, corso Duca degli Abruzzi 24, 10129 Torino, Italy. [2]These authors jointly supervised this work: Michele Re Fiorentin, Giancarlo Cicero. ✉e-mail: michele.bianchi@polito.it

phenomenon still require a detailed elucidation. In this regard, while ab initio simulations have been considered a powerful tool for understanding molecular adsorption and electron transfer, most theoretical works on WS_2 MLs have so far relied on charge population analysis (CPA), without explicitly considering the intrinsic *n*-doping of the MLs[14,16,37]. Moreover, results are rarely correlated with the analysis of band diagrams and frequently suggest carrier transfers even when the band occupation of the ML is not affected by molecular adsorption. Indeed, calculations based on CPA often highlight the transfer of negligible electron fractions, whose values strongly depend on the specific partition scheme adopted and cannot be easily converted into reasonable variations of carrier concentrations. This calls for an alternative, general, and physically sound approach to the problem, in which the intrinsic *n*-type of WS_2, a variable defect density, and the presence of various adsorbed species at different coverages are taken into account. The outcome would be compatible with an evident change in the band occupancy and would forecast measurable variations of the electronic and optical properties.

In this work, by means of ab initio simulations based on Density Functional Theory (DFT), we propose an effective approach for the analysis of the electron transfer mechanism underlying the PL enhancement in WS_2 MLs exposed to air. Firstly, the presence of S vacancies and, above all, the intrinsic *n*-type character of WS_2 are explicitly considered in the adsorption process, improving on previous works. Secondly, we apply the formalism commonly adopted for charged defects in semiconductors[38,39] to jointly describe the process of molecular adsorption and electron transfer in *n*-type samples. This way, the electron transfer from the ML conduction band (CB) to extrinsic surface states introduced by adsorbed molecules can be solidly determined from the variations of the Fermi level of the material. We find that the adsorption of O_2 on the pristine surface of WS_2 MLs is unable to mediate an electron transfer toward the molecule. Only when O_2 is physisorbed on V_S and the ML is *n*-doped, it is possible to have a charge transfer able to modify the WS_2 electronic properties.

This work offers a more accurate picture of molecular physisorption and charge transfer on WS_2 MLs, elucidating the behavior of ML samples exposed to air, while providing an effective and general method to evaluate the variations of the carrier concentrations in nanomaterials with adsorbed molecules.

Results

The impact of O_2 on the electronic and optical properties of WS_2 MLs has been attributed to the variation of the free electron concentration in the material upon molecular physisorption. Given the *n*-type nature of WS_2 MLs, the most commonly invoked mechanism involves the transfer of electrons from the CB of WS_2 to localized O_2 electronic states, leading to a depletion of free electrons in the material[40].

Fundamentally, the process of charge transfer between the electronic bands of the 2D material and the surface states introduced by the adsorbed molecules closely mimics the ionization of dopants in semiconductors. Similarly to the in-gap defect states of a dopant that can acquire/release carriers from/to the bands of the host material, adsorbed molecules can be responsible for in-gap extrinsic surface states whose occupancy changes upon charge transfer with the bands of the 2D material. At equilibrium, the final free electron concentration in the monolayer results from the interplay between the density of states of the pristine material and the occupancy of all possible defect states and/or molecular surface states. The Fermi level of the system is obtained by imposing the charge neutrality condition between the monolayer and all possible dopants and adsorbed species, as detailed in the "Methods" section. In this framework, the occupancy of the in-gap states naturally emerges from the balance between the free energies of formation of dopants/adsorbed species in their neutral and charged states[38,39].

Configurations and Gibbs free energies of formation in neutral and charged states

We apply the discussed framework to the problem of charge modulation by molecular adsorption on WS_2 MLs. We consider the presence of S vacancies, the most abundant defects in WS_2 [41–47], and different molecules (i.e., O_2 and N_2) adsorbed either on the pristine surface, $\circledast$, or on V_S, in their neutral and negatively charged states since they generate acceptor states[16,29]. The bare V_S and the adsorbed molecules are modeled in a unified approach as point defects capable of generating in-gap states. Their ability to trap free electrons is then explored.

The list of considered systems, generically labeled as configurations, is reported in Table 1. The stability of each configuration, *C*, in either the neutral or charged state, as a function of the Fermi level of the host material, E_F, is obtained from the corresponding charge transition level[48], as described in the "Methods" section. Since the in-gap states observed in all configurations have acceptor nature, we focus on charge transition levels $\epsilon_{0/-1}[C]$: the neutral state of configuration *C* is more stable (i.e., the in-gap states do not tend to trap extra electrons) for $E_F < \epsilon_{0/-1}[C]$, while the negative state is the most stable (i.e., the in-gap states acquire one additional electron) for $E_F > \epsilon_{0/-1}[C]$. We reference the values of E_F and $\epsilon_{0/-1}[C]$ to the valence band maximum, E_{VBM}, of pristine WS_2 ML.

O_2 physisorption is initially investigated on the pristine basal plane ($C = \circledast + O_2$). Similarly to other works[16,25], the most stable adsorption site on the pristine basal plane is above the W atom, with the O_2 molecule almost parallel to the surface. The detailed description of the adsorption geometry is reported in Supplementary Note 1 in the Supplementary Information and the complete geometrical structures are available at[49]. The adsorption energy in the neutral configuration is ~−100 meV. On the contrary, the negatively charged configuration does not yield stable results (i.e., positive adsorption energy, as reported in Table 1), indicating that O_2 adsorbed on the pristine basal plane cannot be regarded as a negatively charged point defect. In other words, in this arrangement, O_2 cannot effectively capture free electrons from the material CB and localize them in surface states arising from the adsorbed molecule, rendering it ineffective in influencing the optoelectronic properties of WS_2 MLs. This evidence is confirmed by the charge transition level of O_2 adsorbed on pristine, $\epsilon_{0/-1}[\circledast + O_2] = 2.15$ eV, that falls above the conduction band minimum $E_{CBm} = 1.89$ eV, referenced to E_{VBM}. Hence, in the following analysis, we will solely focus on the configurations that involve V_S.

We consider the configurations $C = V_S, V_S + M$, with $M = O_2, N_2$, in the neutral, C^0, and negatively charged, C^-, states. More details about the adsorption geometries of O_2 and N_2 molecules on V_S site are reported in Supplementary Note 1 in the Supplementary Information. The charge transition levels $\epsilon_{0/-1}[C]$ and the Gibbs free energies of formation $\Delta G^f[C^q]$ referenced to the formation of the neutral vacancy, V_S^0 (see "Methods" section), are reported in Fig. 1a. Noticeably, V_S^- undergoes a Jahn-Teller distortion with the breaking of the D_{3h} symmetry (i.e., the three W atoms surrounding the defect site are no more equivalent and equally spaced, as better shown in Supplementary Note 1 in the Supplementary Information), that further stabilizes the defect, as identified by Tan et al.[50]. As reported in the "Methods" section, here N_2 and O_2 gases are assumed at room temperature and with partial pressures $p_{N_2} = 0.8$ atm and $p_{O_2} = 0.2$ atm, as measured in air at standard conditions. ΔG^f is higher for $(V_S + N_2)^0$ and $(V_S + O_2)^0$ than V_S^0. Despite the slightly stronger adsorption of O_2 than N_2 on V_S^0, as shown in Table 1, the larger entropy loss in O_2 adsorption results in $\Delta G^f[(V_S + O_2)^0] > \Delta G^f[(V_S + N_2)^0] \gtrsim \Delta G^f[V_S^0]$. However, for $q = -1$ we have $\Delta G^f[(V_S + N_2)^-] \gtrsim \Delta G^f[V_S^-] > \Delta G^f[(V_S + O_2)^-]$ for all values of E_F. The variation in the stability ordering in passing from $q = 0$ to $q = -1$ reflects the more negative adsorption energy of O_2 adsorption on V_S^-, as shown in Table 1. It is important to notice that, while the adsorption of O_2 on V_S is stronger in the negative state, the adsorption energy of N_2 on V_S remains nearly the same for both $q = 0$ and $q = -1$, (see Table 1). Consequently, the charge transition levels of the bare V_S and $V_S + N_2$ are almost coincident. On the contrary, due to the stronger interaction between O_2 and V_S in the negatively charged state, $\epsilon_{0/-1}[V_S + O_2]$ is shifted by approximately 80 meV below the charge transition levels $\epsilon_{0/-1}[V_S + N_2] \simeq \epsilon_{0/-1}[V_S]$. As a result, while N_2 on V_S is unable to trap more electrons than the bare V_S, the O_2 interaction with V_S favors the negatively charged state over the neutral one and promotes the trapping of free electrons.

From ΔG^f, we can derive the fraction θ of vacancy sites covered with O_2 or N_2, in neutral and charged state, as a function of E_F, see "Methods" section. In Fig. 1b,c, and d, respectively, we distinguish the cases in which WS_2 is in a vacuum, in an N_2 environment ($p_{N_2} = 1$ atm) and in air ($p_{N_2} = 0.8$ atm, $p_{O_2} = 0.2$ atm). Notably, in Fig. 1b,c, the cumulative fraction of V_S (with and without adsorbates) in the $q = 0$ state, θ^0 (solid black line), and in the $q = -1$ state, θ^- (dashed black line), cross each other almost exactly at the same value $E_F \simeq \epsilon_{0/-1}[V_S]$. In contrast, in Fig. 1d (air environment), the intersection is shifted to lower values of E_F. In intrinsic samples, where $E_F \simeq E_{gap}/2 \ll \epsilon_{0/-1}[V_S]$, all configurations are found in their neutral state, $\theta^0 = 100\%$, independently of the surrounding environment. In this condition, no transfer of electrons to surface-localized electronic states occurs. However, as E_F increases, θ^- grows faster in samples exposed to air. This implies that, with increasing n-doping, WS_2 MLs in an air environment exhibit a greater ability than those in a vacuum or in N_2 to trap free electrons in localized states, thanks to O_2 adsorption on V_S.

Modulations in electron concentration and their impact on photoluminescence

To confirm that a decrease in the free electron concentration, n_e, specifically occurs in n-doped samples from the trapping of free electrons in localized surface states induced by O_2 adsorption, we compute the equilibrium Fermi levels of n-doped MLs in different environments. As reported in the "Methods" section, we take into account the n-doped nature of WS_2 MLs by explicitly including in the charge balance an electron density source, ρ. We also account for the presence of a certain surface density of V_S, n_{V_S}, which is typically introduced in the ML during the synthesis process[29]. The charge balance condition, Eq. (5) in the "Methods" section, is then solved in controlled environments: in a vacuum, in N_2 atmosphere and in air ($N_2 + O_2$) at standard conditions, as commonly performed in experiments[14,18,19]. Our model relies then on two free parameters, n_{V_S} and ρ, which are varied within reasonable ranges ($10^{10} \div 10^{13}$ cm^{-2}), extrapolated from experimental results in the literature[22,51–55]. From the equilibrium Fermi level, obtained from the solution of the charge balance constraint at various (n_{V_S}, ρ) in each environment, we derive the corresponding free electron density in the sample.

In Fig. 2a,b, we report the ratio of the electron density of WS_2 MLs in a gas atmosphere, n_e^{gas}, to the electron density in a vacuum, n_e^{vac}. In Fig. 2a the gas is air ($N_2 + O_2$), while in Fig. 2b it is N_2. We can notice that in air the free electron density can be reduced by up to a factor of two. The largest impact occurs in systems with high vacancy concentration and relatively milder doping (top-left side of the map). Indeed, $n_{V_S} \gg \rho$ ensures that a sizeable fraction of free electrons can be trapped in localized surface states, thus effectively reducing n_e. Conversely, a substantial intrinsic electron concentration, as seen on the right side of the map, results in a less noticeable reduction of n_e due to O_2 adsorption on V_S. This is because high ρ values make the bare S vacancy an effective acceptor defect, capable of trapping electrons on its own. In an N_2 atmosphere, as shown in Fig. 2b, n_e remains largely unchanged compared to the vacuum case.

Given that the majority of the experimental evidence on the impact of air on the optoelectronic properties of WS_2 MLs comes from PL measurements, it is convenient to display the obtained results in terms of the ratio between the intensities of the peaks corresponding to the neutral exciton, X^0, and the negative trion, X^-, in the PL spectrum. Indeed, as explained in the "Methods" section, the intensity ratio $r^{env}_{X^0/X^-}$, in a certain environment, is inversely proportional to the corresponding free electron density weighed by the Fermi level. It is then possible to define a function $R_{gas/vac} = r^{gas}_{X^0/X^-}/r^{vac}_{X^0/X^-}$ that provides us with the relative enhancement of

Table 1 | Charge transition levels $\epsilon_{0/-1}$ between neutral and negatively charged states and molecular adsorption energies E_{ads} (when applicable)

Configuration	$\epsilon_{0/-1}$ (eV)	E_{ads} (meV)	
		$q = 0$	$q = -1$
V_S	1.75 (8)	–	–
⊛ $+O_2$	2.15 (4)	−100	>0
$V_S + O_2$	1.69 (9)	−150	−240
$V_S + N_2$	1.75 (6)	−140	−150

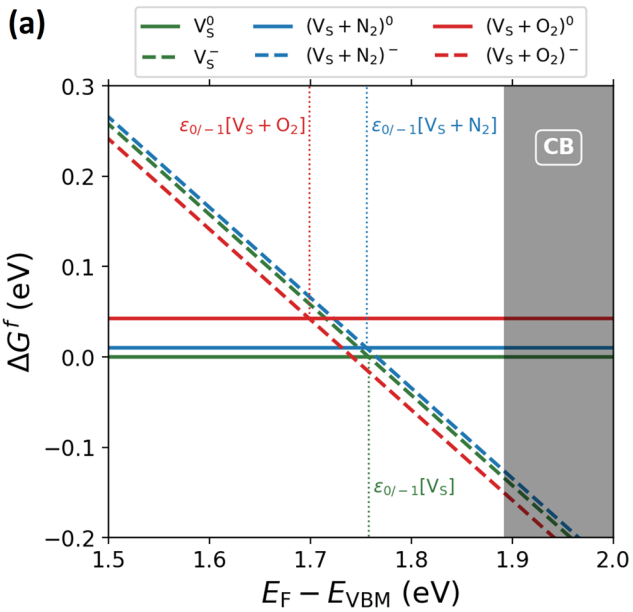

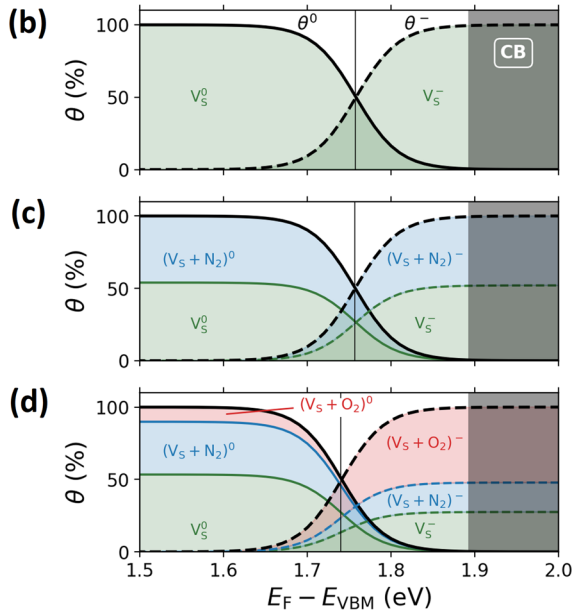

Fig. 1 | Gibbs free energies and associated cumulative fraction sites of V_S for the different configurations. a Gibbs free energies of formation in the neutral (solid lines) and negatively charged (dashed lines) states of bare V_S (green), $(V_S + N_2)$ (blue) and $(V_S + O_2)$ (red). The respective charge transition levels $\epsilon_{0/-1}$ are marked by vertical segments. **b–d** cumulative fraction of V_S sites in neutral, θ^0 (solid black line) or negatively charged, θ^- (dashed black line) state, in different environmental conditions. **b** vacuum, **c** inert N_2 atmosphere, **d** air ($N_2 + O_2$) atmosphere. The relative contributions of bare V_S, $(V_S + N_2)$ and $(V_S + O_2)$ to the cumulative fraction of V_S are shown by green, blue, and red areas, respectively.

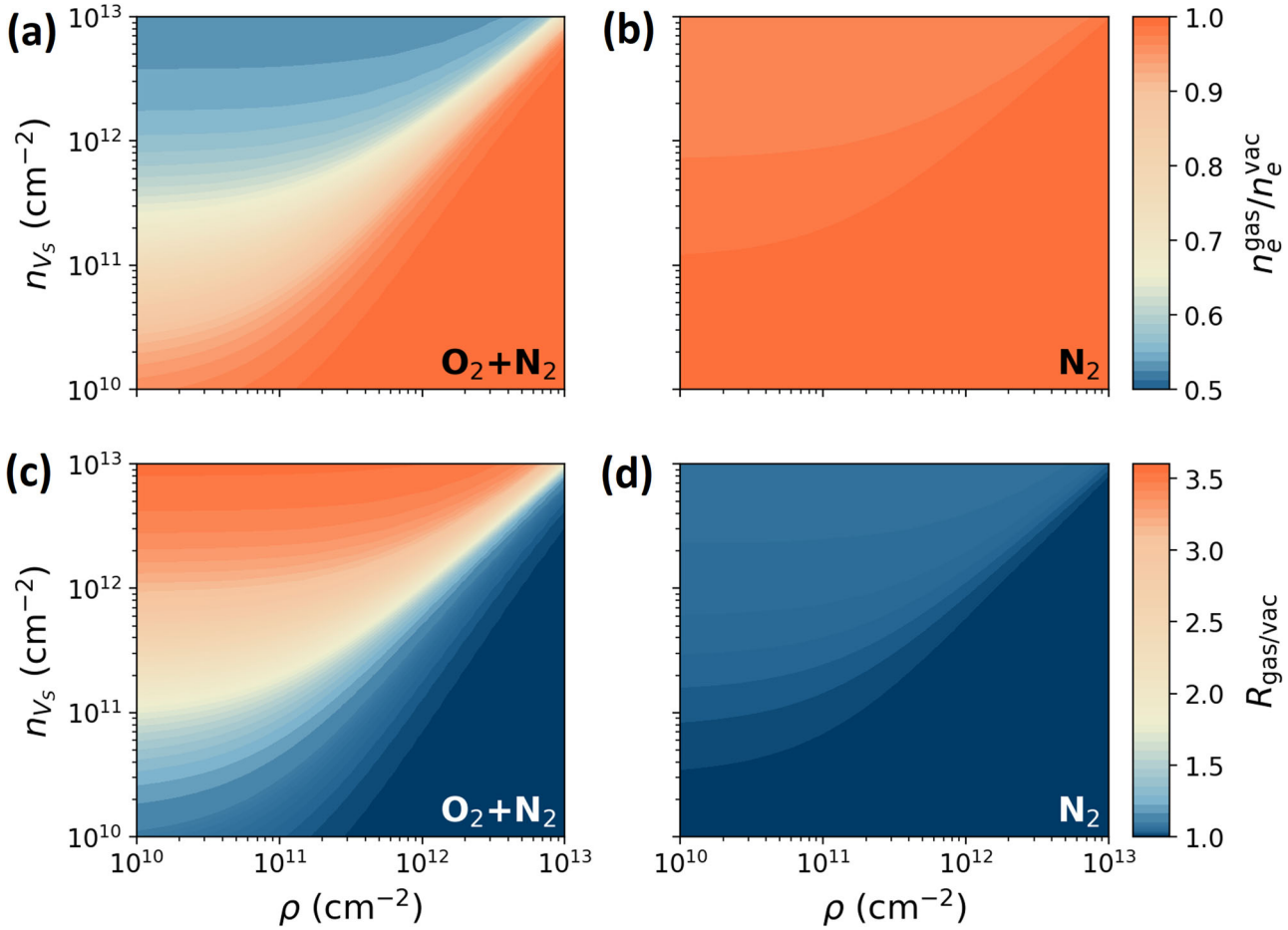

Fig. 2 | Relative variations in electron concentration and PL peak intensity in different "gas" environment. Upper panels Ratios n_e^{gas}/n_e^{vac} where "gas" is air in **a** and inert N_2 in **b**. Lower panels Relative enhancement of the X^0 peak with respect to X^- between a gas atmosphere and the vacuum. Air in **c** and N_2 in **d**.

the X^0 peak with respect to X^- between a gas atmosphere and the vacuum. The parametric analyses of $R_{gas/vac}$ on (n_{V_S}, ρ) in air and in the inert N_2 atmosphere are reported in Fig. 2c, d, respectively.

From Fig. 2c we notice that, in the presence of O_2, the neutral exciton peak is up to about 3.5 times more intense, with respect to the negative trion one, than in the vacuum case. This is in good agreement with the experimental results[18,21], which show similar enhancements of the neutral exciton peaks in samples exposed to air. As in Fig. 2a,b, the largest effect occurs in samples with high densities of V_S. This outcome is also in line with the experimental data showing that MLs in which additional V_S are created are more responsive to the presence of oxygen[14,20]. It is crucial to emphasize that the enhancement of X^0 is exclusively observed in the presence of air. In an inert atmosphere such as N_2 gas, Fig. 2d, the maximum enhancement is approximately $R_{gas/vac} \simeq 1.1$, proving that the key to the modulation of the electronic properties of WS_2 MLs is O_2 physisorption on V_S. We can therefore conclude that, by stabilizing the negatively charged state, it is the physisorption of O_2 on V_S in *n*-doped WS_2 MLs that induces an electron transfer from the CB of WS_2 to localized surface states and the corresponding reduction of the free electron density, with sizeable impact on the optoelectronic properties of the material.

Analysis of the electronic properties

The electron transfer mechanism can be further investigated by studying the electronic properties of the different configurations of O_2 physisorption. For reference, the band diagrams and the Partial Densities of States (PDOS) of the bare V_S, in neutral and negative charged states, are reported in Fig. 3a,b, respectively. The electronic signature of V_S is a couple of energetically degenerate empty in-gap states. Upon addition of an electron, a defect state turns to be occupied (acceptor nature), removing the degeneracy of the energy levels.

The analysis of the electronic band structure of O_2 adsorbed on pristine neutral ML, as depicted in Fig. 3c, shows a spin-down, anti-bonding state associated with O_2 (solid blue peak in the PDOS panel), which corresponds to the LUMO of the isolated molecule. This state lies within the electronic gap of WS_2, in agreement with findings reported elsewhere[16], and remains completely unoccupied, despite the interaction with the ML. Hence, when O_2 is physisorbed on the pristine basal plane of intrinsic WS_2 MLs, no electron transfer from the TMD to the molecule occurs. This result contradicts the conclusions drawn in other studies[16,25]. In the negatively charged state, Fig. 3d, the anti-bonding state of O_2 upshifts to higher energies inside the CB. The shift of the Fermi level causes the partial occupation of the lowest states of the CB of WS_2 (dotted red and blue lines in the PDOS panel), but the anti-bonding state of the O_2 molecule still remains unoccupied. Consistently with the conclusion drawn from the positive adsorption energy and the analysis of the charge transition level in Table 1, the adsorption of O_2 on the pristine basal plane does not facilitate the electron transfer from the ML to the molecule and does not lead to a reduction in the free electron density.

The presence of sulphur vacancies alters this picture. O_2 adsorbs more strongly on neutral V_S than on the pristine basal plane, see Table 1. When WS_2 is intrinsic, Fig. 3e, the anti-bonding state of O_2 (solid blue peak in the PDOS panel) is located inside the gap region, empty and disjointed from the defect states of V_S (dotted red and blue peaks in the PDOS). The energy levels of V_S states are almost unaltered with respect to the configuration reported in Fig. 3a. Indeed, the PDOS shows that there is almost no contribution of the O species to the electron density peaks related to the V_S electronic states. On the contrary, when an extra electron is added to the

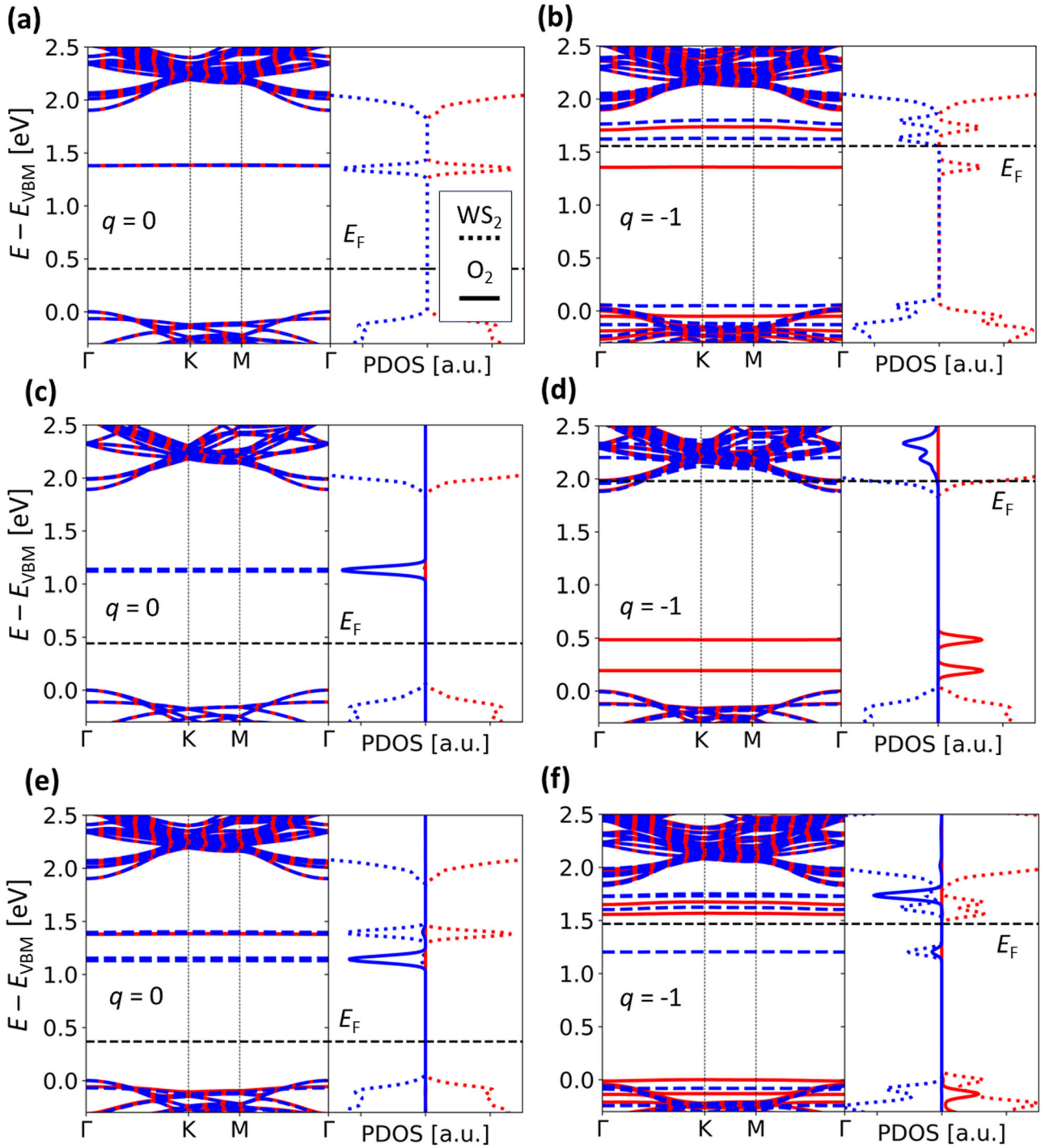

Fig. 3 | Band diagrams and PDOS of bare V_S and different configurations of O_2 on WS_2 ML in a 6 × 6 supercell. **a** bare V_S in the neutral ML, **b** bare V_S in the negative charged ML, **c** O_2 on the pristine neutral ML, **d** O_2 on the pristine negative charged ML, **e** O_2 on the neutral V_S, **f** O_2 on the negatively charged V_S. Red and blue colors represent spin up and spin down states, respectively. Solid and dotted lines in the PDOS panels represent O_2 and WS_2 contributions, respectively. Energies are referred to the valence band maximum (E_{VBM}). The Fermi level E_F is reported as a black dashed line.

system, Fig. 3f, a complete rearrangement of the in-gap states occurs. As in Fig. 3b, the lowest in-gap state is occupied and primarily associated to WS_2, but now it also exhibits a significant contribution from O_2, as evident from the PDOS. The extra charge occupies an electronic state that has a contribution from oxygen orbitals, proving that O_2 acquires a partial negative charge. A more detailed analysis of the PDOS, projecting the electronic states onto the different O atomic orbitals (Supplementary Fig. 3 in the Supplementary Information), reveals that the oxygen contribution to the lowest-energy vacancy state is provided by p_z orbitals with spin-down. This confirms that in $(V_S + O_2)^-$ a charge transfer from the CB to localized in-gap states occurs as a redistribution of the charge density between O_2 and WS_2. This is also supported by the analysis of the square modulus of the wave-function of the lowest-energy electronic state induced by V_S (spin-down component), reported in Fig. 4. When no extra electrons are present (intrinsic semiconductor), the vacancy state is localized in the ML, Fig. 4a. On the contrary, when an extra electron is added, Fig. 4b, the wave-function of the same electronic state is delocalized towards O_2, pointing at an electron transfer towards the molecule.

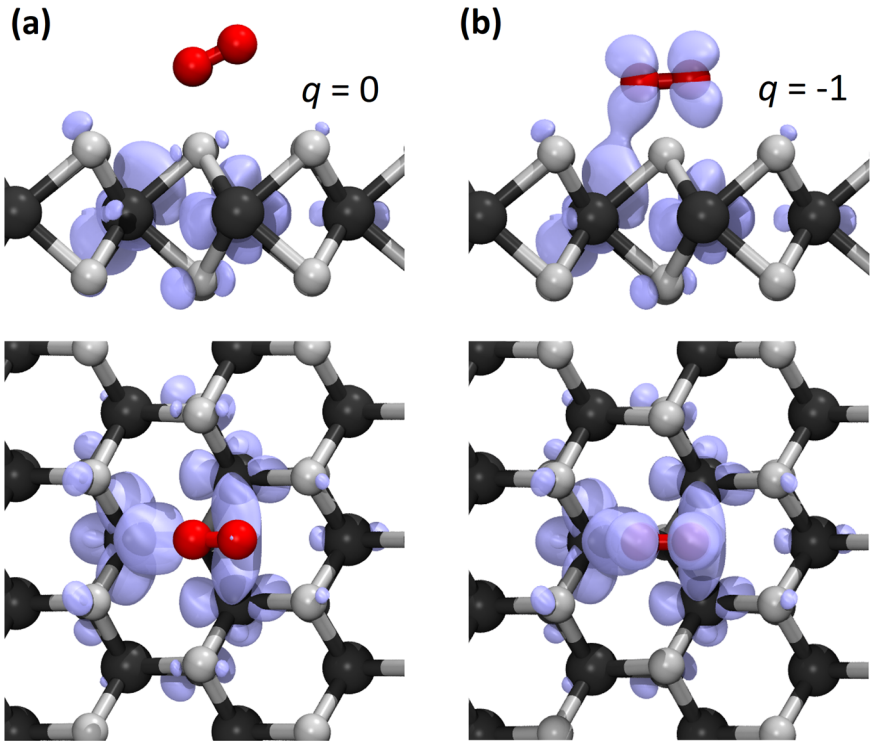

Fig. 4 | Isosurfaces of the square modulus of the wave-function for the lowest V_S in-gap state (spin down contribution) for different cases in WS_2 ML. **a** $(V_S + O_2)^0$, and **b** $(V_S + O_2)^{-1}$. Black, gray, and red spheres represent W, S, and O atoms, respectively.

The evidence that the extra electron tends to be delocalized between the V_S site and the O_2 molecule can be also identified from the average position of the extra charge (Supplementary Table 2 in the Supplementary Information), as computed within the the correction scheme applied to charged supercells (see "Methods" section and Supplementary Note 2 in the Supplementary Information). In contrast to the cases of bare V_S and N_2 on V_S, the charge distribution seems to extend beyond the ML plane and toward the O_2 molecule.

Similar analyses, reported in the Supplementary Information, confirm that no electron delocalization can be identified in N_2 adsorption on V_S. V_S is able to enhance N_2 adsorption, as highlighted by the adsorption energies in Table 1. However, the interaction does not change when the material has extra electrons. The PDOS (Supplementary Fig. 4 in the Supplementary Information) also shows that there is no N contribution to the vacancy states both in the neutral and in the negative charged states. This further proves that V_S selectively enhances the interaction with O_2, while it is insensitive to inert molecules such as N_2.

Comparison with the results from charge population analysis

Finally, we provide some evidence of the shortcomings of conventional CPA, mentioned in the Introduction. CPA aims to assign a partial charge to each atom by employing various methods for partitioning the charge density obtained from ab initio calculations[56]. Commonly, charge transfer in adsorption processes is assessed by comparing the partial charge assigned to the molecule before and after the adsorption, exclusively focusing on the surface of the intrinsic material (i.e., neutral supercells) and considering a single molecule at once[16,25]. The same analysis is hardly ever performed considering the *n*-doped nature of WS_2 MLs (i.e., in negatively charged systems). Moreover, the inclusion of realistic elements, such as a variable intrinsic electron concentration and the co-presence of different gas species, is not a trivial task in the framework of the CPA approach.

As reference, the outcomes of CPA, considering neutral as well as negatively charged systems, are reported in Supplementary Note 6 of the Supplementary Information. Limiting the analysis to the neutral systems, as commonly performed in the literature, results in comparable charge variations on O_2 and N_2, when adsorbed on the same site (both ⊛ and V_S). This fails to distinctly differentiate between active and inert molecules.

The inclusion of an additional electron in the supercell, to mimic *n*-doping, enables the CPA to identify a clear charge transfer in the $(V_S + O_2)^-$ case, in agreement with our proposed method. However, the CPA does not rule out the possibility of small, yet non-negligible, charge transfers in the other configurations. Due to the challenge of associating the assessed charge populations with directly measurable quantities, it remains uncertain if all identified charge transfers significantly affect the optoelectronic properties of WS_2.

Discussion

This study offers a thorough insight into the mechanism governing the modification of the optoelectronic properties of WS_2 MLs when exposed to air. This is achieved through a detailed investigation of molecular adsorption on the ML surface using ab initio simulations. Unlike previous studies, our approach takes into explicit consideration the intrinsic *n*-type nature of WS_2 MLs. This allows for a precise description of how adsorbed molecules can trap electrons in a system that is naturally electron-rich and offers a robust elucidation of the charge transfer mechanism. Going beyond conventional charge population analysis, our methodology adopts the charge balance formalism commonly used in semiconductors with dopants. Our findings reveal that no electron transfer to physisorbed molecules occurs when WS_2 ML is an intrinsic semiconductor. Even in the case of *n*-doped WS_2, we find that O_2 adsorption on the pristine basal plane is ineffective at reducing the free electron concentration. Instead, sulphur vacancies serve as the key O_2 adsorption sites that allow for an effective decrease of the free electron density. These results are supported by consistent analysis of band diagrams and charge densities. The validity of the method is supported by the analysis of the adsorption of an inert molecule, such as N_2, which shows no impact on the WS_2 electron density.

In conclusion, this study not only elucidates the intricate mechanism of O_2 physisorption on WS_2 monolayers, but also provides an effective approach to evaluate the effects of carrier modulation by molecular adsorption, which can be extended to other materials. These findings serve as a promising basis for interpreting experimental variations in the

properties of samples when exposed to air or to controlled environments and have significant implications for the advancement of optoelectronic and gas-sensing technologies based on 2D materials.

Methods

Details of DFT calculations

Calculations are based on spin-polarized DFT, as implemented in Quantum Espresso[57,58]. Norm-conserving pseudopotentials are employed to describe the electron-ion interaction. The adopted exchange-correlation functional is the van der Waals density functional proposed by Hamada (rev-vdW-DF2)[59], based on a Generalized Gradient Approximation (GGA) exchange functional, and able to effectively describe the dispersion forces that characterize physisorption processes. Electronic wave-functions are expanded in plane waves with a cutoff energy of 75 Ry. The Brillouin zone is sampled employing a (5 5 1) Monkhorst-Pack mesh[60] in the case of the WS_2 ML unit cell and consistently reduced for the supercells. The inter-layer spacing between periodic replicas is set to 20 Å. This setting allows to guarantee an effective separation between the adsorbed molecules and the opposite side of the periodic ML image of about 15 Å.

The role of V_S and the adsorption of different molecules are studied considering large supercells (i.e., from 5×5 to 7×7 repetitions of the unit cell) and including a single defect and/or adsorbed molecule. The *n*-type nature of WS_2 MLs is reproduced in the simulations by explicitly adding extra electrons to the supercells, following the treatment proposed in Ref. 18. The full list of simulation parameters can be retrieved from the calculation input files, freely available at[49].

Adsorption energy and Gibbs free energy of formation for neutral and charged states

We compute the electronic adsorption energy of molecule $M = O_2, N_2$ on the adsorption site $* = \circledast$ (pristine) or $* = V_S$ (sulphur vacancy), in the charge states $q = 0, -1$ as

$$E_{\mathrm{ads}}[*+M,q] = E_{\mathrm{tot}}[*+M,q] - E_{\mathrm{tot}}[*,q] - E_M + \Delta E^q_{\mathrm{corr}}, \quad (1)$$

where $E_{\mathrm{tot}}[*+M,q]$ is the energy of the supercell with molecule M adsorbed on site $*$ in the charge state q, $E_{\mathrm{tot}}[*,q]$ is the total energy of the supercell containing the adsorption site $*$ in the charge state q, and E_M is the energy of the isolated molecule M. $\Delta E^q_{\mathrm{corr}}$ is an energy correction term, evaluated according to Ref. 61. More details on the procedure adopted to evaluate these corrections are reported in Supplementary Note 2 of the Supplementary Information.

Extending the approach in refs. 62–64, each configuration C (c.f. Table 1) in the charge state q, is then studied in terms of Gibbs free energy of formation as a function of the Fermi level E_F of the material. The Gibbs free energies of formation are referenced to the formation of neutral V_S as

$$\begin{aligned}\Delta G^{\mathrm{f}}[C^q](E_F, p_M) = \; & G_{\mathrm{tot}}[C^q] - G_{\mathrm{tot}}[V_S^0] - \mu_M(p_M) \\ & + q(E_F + E_{\mathrm{VBM}}) + \Delta E^q_{\mathrm{corr}},\end{aligned} \quad (2)$$

where room temperature $T = 298$ K is assumed. $G_{\mathrm{tot}}[C^q]$ is the total Gibbs free energy of configuration C, in the charge state q. $G_{\mathrm{tot}}[V_S^0]$ is the total Gibbs free energy of neutral V_S, without any adsorbate, used as reference. The term $\mu_M(p_M)$ is the chemical potential of molecule M in the gas phase, at partial pressure p_M, and appears in Eq. (2) only if molecule M is present in configuration C. $\mu_M(p_M)$ is obtained from the total DFT energy, E_M, and the enthalpy and entropy contributions reported in thermochemical tables[65]. E_F is referenced to the valence band maximum E_{VBM} of pristine WS_2 ML. From the Gibbs free energies of formation with $q = 0, -1$, it is possible to obtain the charge transition levels $\epsilon_{0/-1}[C]$ of each configuration and identify the Fermi level range in which each charged state is the most stable[39].

The term $G_{\mathrm{tot}}[C^q]$ of the configurations including an adsorbed molecule are obtained from DFT total energies combined with the enthalpic and entropic contributions of the adsorbed molecule. To more accurately describe the physisorption process, the translational degrees of freedom of the physisorbed molecule are computed within the hindered translator model[66,67]. More details are reported in Supplementary Note 3 of the Supplementary Information.

From the Gibbs free energies of formation, computed in Eq. (2), we obtain the fraction of vacancy sites in configuration $C = V_S, V_S + M$ and charge states $q = 0, -1$ as

$$\theta[C^q] = \frac{1}{Z} e^{-\beta \Delta G^{\mathrm{f}}[C^q]}, \quad (3)$$

where $\beta = 1/k_B T$, with the Boltzmann constant k_B. Z is the partition function including all possible configurations in their different states

$$Z = 1 + e^{-\beta \Delta G^{\mathrm{f}}[V_S^-]} + \sum_{M,q} e^{-\beta \Delta G^{\mathrm{f}}[(V_S+M)^q]}, \quad (4)$$

considering that all ΔG^{f} are referenced to the formation of the neutral V_S ($\Delta G^{\mathrm{f}}[V_S^0] = 0$).

It is known that GGA functionals tend to yield underestimated values of the energy gap, particularly in low-dimensional materials. More advanced exchange-correlation functionals, such as hybrid functionals, can mitigate this problem, albeit at a high computational cost. Yet, the adoption of a more advanced theoretical framework is not essential for the methodology and the results outlined in this study. By employing the HSE06 hybrid functional[68], Singh et al. in Ref. 29 report an $\epsilon_{0/-1}[V_S]$ value in WS_2 ML equal to 1.86 eV, within an energy gap of 2.1 eV. Therefore, $\epsilon_{0/-1}[V_S]$ and, consequently, the other considered charge transition levels computed with the HSE06 functional still lie within the bandgap, as predicted at the GGA level. The distance between the transition levels and the CBm does not impact our results, since the present analysis relies on the relative energy separations between the charge transition levels associated with the various configurations. The spacing between transition levels of localized defects is minimally affected by the band-gap problem and has been shown to be correctly reproduced already at the GGA level[69–71]. Hence, it reasonable to assume that the conclusions of this work will not change if a more accurate description of the band structure is employed.

Charge balance

The variation of free electron concentration, n_e, in WS_2 MLs due to molecular adsorption is evaluated by imposing the charge balance condition, as commonly performed to determine the equilibrium Fermi level in semiconductors with different charged defects[39]. Specifically, the charge balance for a system with a surface density n_{V_S} of sulphur vacancies in the possible configurations $C = V_S, V_S + M$ and charge states $q = 0, -1$, can be written as

$$\begin{aligned}&\rho + n_{V_S} \sum_{C,q} q \frac{1}{Z} e^{-\beta \Delta G^{\mathrm{f}}[C^q](E_F)} = \\ &\int_{E_{\mathrm{CBm}}}^{+\infty} g(E) f_{\mathrm{FD}}(E, E_F) dE - \int_{-\infty}^{E_{\mathrm{VBM}}} g(E)[1 - f_{\mathrm{FD}}(E, E_F)] dE.\end{aligned} \quad (5)$$

$\Delta G^{\mathrm{f}}[C^q](E_F)$ is the Gibbs free energy of formation as defined in Eq. (2), $g(E)$ is the density of states of the pristine WS_2 ML and f_{FD} is the Fermi-Dirac distribution. Values of n_{V_S} for WS_2 MLs can be retrieved from experimental data[22,51,52]. Depending on the different synthesis conditions, they typically range from 10^{10} to 10^{13} cm^{-2}.

Since the origin of the intrinsic *n*-type character of WS_2 samples is still debated, and might be associated with electron transfer processes from the substrate[10,72,73], donor defects are not explicitly considered in the charge balance, as performed elsewhere[38]. Instead, we introduce in Eq. (5) a source term of free electron density, ρ, that mimics the *n*-type of WS_2 samples. Typical values of ρ can be obtained from experimental data in the literature and vary between 10^{10} and 10^{13} cm^{-2} (refs. 22,53–55).

PL peak intensities

The free electron density in the ML influences the PL of the material, altering the ratio between the intensity of the PL peak associated to the negative trion $I(X^-)$ and the intensity $I(X^0)$ of the neutral exciton peak. Indeed, we have[74,75]

$$r_{X^0/X^-} = \frac{I(X^0)}{I(X^-)} \propto \frac{e^{-\beta E_b}}{n_e} \propto \frac{e^{-\beta E_F}}{n_e}, \quad (6)$$

where E_b is the trion binding energy, proportional to the Fermi level E_F [76]. Hence, the PL in a gas atmosphere can be compared to that in a vacuum through the ratio

$$R_{gas/vac} \equiv \frac{r^{gas}_{X^0/X^-}}{r^{vac}_{X^0/X^-}} = \frac{e^{-\beta E_F^{gas}}}{n_e^{gas}} \frac{n_e^{vac}}{e^{-\beta E_F^{vac}}} = \frac{n_e^{vac}}{n_e^{gas}} e^{\beta(E_F^{vac} - E_F^{gas})}, \quad (7)$$

where the label gas can be either air or N_2. The dependence of n_e and E_F on ρ and n_{V_S} is implied.

Data availability

Computational data underlying this study can be accessed via the ioChem-BD data repository[77] at https://doi.org/10.19061/iochem-bd-6-338[49].

Code availability

All codes used in this work are open-source. DFT calculations were performed with Quantum ESPRESSO, freely available at https://github.com/QEF/q-e. The *sxdefectalign2d* code, used for correcting the energies of charged defects, can be freely obtained from https://sxrepo.mpie.de.

Received: 6 November 2023; Accepted: 15 March 2024;
Published online: 28 March 2024

References

1. Chakraborty, C., Vamivakas, N. & Englund, D. Advances in quantum light emission from 2D materials. *Nanophotonics* **8**, 2017–2032 (2019).
2. Kang, S. et al. 2D semiconducting materials for electronic and optoelectronic applications: potential and challenge. *2D Materials* **7**, 022003 (2020).
3. Cheng, Z. et al. 2D materials enabled next-generation integrated optoelectronics: from fabrication to applications. *Adv. Sci.* **8**, 2003834 (2021).
4. Lackner, L. et al. Tunable exciton-polaritons emerging from WS_2 monolayer excitons in a photonic lattice at room temperature. *Nat. Commun.* **12**, 4933 (2021).
5. Gupta, S., Wu, W., Huang, S. & Yakobson, B. I. Single-photon emission from two-dimensional materials, to a brighter future. *J. Phys. Chem. Lett.* **14**, 3274–3284 (2023).
6. Gutiérrez, H. R. et al. Extraordinary room-temperature photoluminescence in triangular WS_2 monolayers. *Nano Lett.* **13**, 3447–3454 (2013).
7. Pace, S. et al. Thermal stability of monolayer WS_2 in BEOL conditions. *J. Phys. Mater.* **4**, 024002 (2021).
8. Xiang, D. & Liu, T. Monolayer transistors at wafer scales. *Nat. Electron.* **4**, 868–869 (2021).
9. Zeng, H. et al. Recent developments in CVD growth and applications of 2D transition metal dichalcogenides. *Front. Phys.* **18**, 53603 (2023).
10. Kang, Y. & Han, S. An origin of unintentional doping in transition metal dichalcogenides: the role of hydrogen impurities. *Nanoscale* **9**, 4265–4271 (2017).
11. Şar, H. et al. A comparative device performance assesment of CVD grown MoS_2 and WS_2 monolayers. *J. Mater. Sci.-Mater. Electron.* **29**, 8785–8792 (2018).
12. Hu, Z. et al. The role of oxygen atoms on excitons at the edges of monolayer WS_2. *Nano Lett.* **19**, 4641–4650 (2019).
13. Atkin, P. et al. Laser exposure induced alteration of WS_2 monolayers in the presence of ambient moisture. *2D Materials* **5**, 015013 (2017).
14. Tongay, S. et al. Broad-range modulation of light emission in two-dimensional semiconductors by molecular physisorption gating. *Nano Lett.* **13**, 2831–2836 (2013).
15. Hou, C. et al. Photoluminescence of monolayer MoS_2 modulated by water/O_2/laser irradiation. *Phys. Chem. Chem. Phys.* **23**, 24579–24588 (2021).
16. Bui, V. Q., Pham, T.-T., Le, D. A., Thi, C. M. & Le, H. M. A first-principles investigation of various gas (CO, H_2O, NO, and O_2) absorptions on a WS_2 monolayer: stability and electronic properties. *J. Phys.-Condes. Matter* **27**, 305005 (2015).
17. Deb, S. et al. Effect of oxygen adsorption on electrical and thermoelectrical properties of monolayer MoS_2. *Phys. Rev. Appl.* **14**, 034030 (2020).
18. Klement, P., Steinke, C., Chatterjee, S., Wehling, T. O. & Eickhoff, M. Effects of the fermi level energy on the adsorption of O_2 to monolayer MoS_2. *2D Materials* **5**, 045025 (2018).
19. Zhang, H. et al. Disentangling oxygen and water vapor effects on optoelectronic properties of monolayer tungsten disulfide. *Nanoscale* **12**, 8344–8354 (2020).
20. Li, Y. et al. Unraveling the synergetic mechanism of physisorption and chemisorption in laser-irradiated monolayer WS_2. *Nano Res.* **14**, 4274–4280 (2021).
21. Birmingham, B. et al. Spatially-resolved photoluminescence of monolayer MoS_2 under controlled environment for ambient optoelectronic applications. *ACS Appl. Nano Mater.* **1**, 6226–6235 (2018).
22. Rao, R. et al. Dynamics of cleaning, passivating and doping monolayer MoS_2 by controlled laser irradiation. *2D Materials* **6**, 045031 (2019).
23. Oh, H. M. et al. Photochemical reaction in monolayer MoS_2 *via* correlated photoluminescence, raman spectroscopy, and atomic force microscopy. *ACS Nano* **10**, 5230–5236 (2016).
24. Zhao, S. et al. Substitutional oxygen activated photoluminescence enhancement in monolayer transition metal dichalcogenides. *Sci. China-Mater.* **65**, 1034–1041 (2022).
25. Zhou, C., Yang, W. & Zhu, H. Mechanism of charge transfer and its impacts on Fermi-level pinning for gas molecules adsorbed on monolayer WS_2. *J. Chem. Phys.* **142**, 214704 (2015).
26. Yue, Q., Shao, Z., Chang, S. & Li, J. Adsorption of gas molecules on monolayer MoS_2 and effect of applied electric field. *Nanoscale Res. Lett.* **8**, 425 (2013).
27. Leenaerts, O., Partoens, B. & Peeters, F. M. Adsorption of H_2O, NH_3, CO, NO_2, and NO on graphene: a first-principles study. *Phys. Rev. B* **77**, 125416 (2008).
28. Salomone, M., Re Fiorentin, M., Cicero, G. & Risplendi, F. Point defects in two-dimensional indium selenide as tunable single-photon sources. *J. Phys. Chem. Lett.* **12**, 10947–10952 (2021).
29. Singh, A. & Singh, A. K. Atypical behavior of intrinsic defects and promising dopants in two-dimensional WS_2. *Phys. Rev. Mater.* **5**, 084001 (2021).
30. Re Fiorentin, M., Kiprono, K. K. & Risplendi, F. Substitutional impurities in monolayer hexagonal boron nitride as single-photon emitters. *Nanomater. Nanotechnol.* **10**, 184798042094934 (2020).
31. Salomone, M., Raffone, F., Re Fiorentin, M., Risplendi, F. & Cicero, G. Stability and bandgap engineering of $In_{1-x}Ga_xSe$ monolayer. *Nanomaterials* **12**, 515 (2022).
32. Verma, A. K., Raffone, F. & Cicero, G. Prediction of the structural and electronic properties of $Mo_xTi_{1-x}S_2$ monolayers via first principle simulations. *Nanomater. Nanotechnol.* **10**, 184798042095509 (2020).
33. Ouahrani, T. et al. Effect of intrinsic point defects on the catalytic and electronic properties of Cu_2WS_4 single layer: Ab initio calculations. *Phys. Rev. Mater.* **7**, 025403 (2023).

34. Yao, X. et al. Activated basal planes of WS_2 by intrinsic defects as catalysts for the electrocatalytic nitrogen reduction reaction. *J. Mater. Chem. A* **7**, 25961–25968 (2019).
35. Fan, F. R., Wang, R., Zhang, H. & Wu, W. Emerging beyond-graphene elemental 2D materials for energy and catalysis applications. *Chem. Soc. Rev.* **50**, 10983–11031 (2021).
36. Li, H., Huang, M. & Cao, G. Markedly different adsorption behaviors of gas molecules on defective monolayer MoS_2: a first-principles study. *Phys. Chem. Chem. Phys.* **18**, 15110–15117 (2016).
37. Gustafson, J. K., Wines, D., Gulian, E., Ataca, C. & Hayden, L. M. Positive and negative photoconductivity in monolayer MoS_2 as a function of physisorbed oxygen. *J. Phys. Chem. C* **125**, 8712–8718 (2021).
38. Yu, Y. G., Zhang, X. & Zunger, A. Natural off-stoichiometry causes carrier doping in half-heusler filled tetrahedral structures. *Phys. Rev. B* **95**, 085201 (2017).
39. Zunger, A. & Malyi, O. I. Understanding doping of quantum materials. *Chem. Rev.* **121**, 3031–3060 (2021).
40. Zhang, X., Shao, Z., Zhang, X., He, Y. & Jie, J. Surface charge transfer doping of low dimensional nanostructures toward high performance nanodevices. *Adv. Mater.* **28**, 10409–10442 (2016).
41. Bianchi, M. G., Risplendi, F., Re Fiorentin, M. & Cicero, G. Engineering the electrical and optical properties of WS_2 monolayers via defect control. *Adv. Sci.* **11**, 2305162 (2024).
42. Lin, Y.-C. et al. Revealing the atomic defects of WS_2 governing its distinct optical emissions. *Adv. Funct. Mater.* **28**, 1704210 (2018).
43. Liu, H., Wang, C., Liu, D. & Luo, J. Neutral and defect-induced exciton annihilation in defective monolayer WS_2. *Nanoscale* **11**, 7913–7920 (2019).
44. Kastl, C. et al. Effects of defects on band structure and excitons in WS_2 revealed by nanoscale photoemission spectroscopy. *ACS Nano* **13**, 1284–1291 (2019).
45. Maksov, A. et al. Deep learning analysis of defect and phase evolution during electron beam-induced transformations in WS_2. *npj Comput. Mater.* **5**, 12 (2019).
46. Cavallini, M. & Gentili, D. Atomic vacancies in transition metal dichalcogenides: properties, fabrication, and limits. *ChemPlusChem* **87**, e202100562 (2022).
47. Thomas, J. C. et al. Autonomous scanning probe microscopy investigations over WS_2 and Au{111}. *npj Comput. Mater.* **8**, 99 (2022).
48. Freysoldt, C. et al. First-principles calculations for point defects in solids. *Rev. Mod. Phys.* **86**, 253–305 (2014).
49. Bianchi, M. G., Risplendi, F., Re Fiorentin, M. & Cicero, G. *Addressing The Effects Of Gas Adsorption On Monolayers Beyond Charge Population Analysis: The Case Of WS_2*. IoChem-BD database https://doi.org/10.19061/iochem-bd-6-338 (2024).
50. Tan, A. M. Z., Freysoldt, C. & Hennig, R. G. Stability of charged sulfur vacancies in 2D and bulk MoS_2 from plane-wave density functional theory with electrostatic corrections. *Phys. Rev. Mater.* **4**, 064004 (2020).
51. Rosenberger, M. R., Chuang, H.-J., McCreary, K. M., Li, C. H. & Jonker, B. T. Electrical characterization of discrete defects and impact of defect density on photoluminescence in monolayer WS_2. *ACS Nano* **12**, 1793–1800 (2018).
52. Chu, Z. et al. Unveiling defect-mediated carrier dynamics in monolayer semiconductors by spatiotemporal microwave imaging. *Proc. Natl. Acad. Sci. USA.* **117**, 13908–13913 (2020).
53. Demeridou, I. et al. Spatially selective reversible charge carrier density tuning in WS_2 monolayers via photochlorination. *2D Materials* **6**, 015003 (2018).
54. Wang, S. Y., Ko, T. S., Huang, C. C., Lin, D. Y. & Huang, Y. S. Optical and electrical properties of MoS_2 and Fe-doped MoS_2. *Jpn J. Appl. Phys.* **53**, 04EH07 (2014).
55. Zhang, S. et al. Controllable, wide-ranging n-doping and p-doping of monolayer group 6 transition-metal disulfides and diselenides. *Adv. Mater.* **30**, 1802991 (2018).
56. Cho, M. et al. The atomic partial charges arboretum: trying to see the forest for the trees. *ChemPhysChem* **21**, 688–696 (2020).
57. Giannozzi, P. et al. Quantum espresso: a modular and open-source software project for quantum simulations of materials. *J. Phys.-Condes. Matter* **21**, 395502 (2009).
58. Giannozzi, P. et al. Advanced capabilities for materials modelling with quantum espresso. *J. Phys.-Condes. Matter* **29**, 465901 (2017).
59. Hamada, I. van der Waals density functional made accurate. *Phys. Rev. B* **89**, 121103 (2014).
60. Monkhorst, H. J. & Pack, J. D. Special points for brillouin-zone integrations. *Phys. Rev. B* **13**, 5188–5192 (1976).
61. Freysoldt, C. & Neugebauer, J. First-principles calculations for charged defects at surfaces, interfaces, and two-dimensional materials in the presence of electric fields. *Phys. Rev. B* **97**, 205425 (2018).
62. Alkauskas, A., Broqvist, P. & Pasquarello, A. Charge state of the O_2 molecule during silicon oxidation through hybrid functional calculations. *Phys. Rev. B* **78**, 161305 (2008).
63. Bonapasta, A. A. & Filippone, F. Photocatalytic reduction of oxygen molecules at the (100) TiO_2 anatase surface. *Surf. Sci.* **577**, 59–68 (2005).
64. Filippone, F., Mattioli, G. & Bonapasta, A. A. Reaction intermediates and pathways in the photoreduction of oxygen molecules at the (101) TiO_2 (anatase) surface. *Catal. Today* **129**, 169–176 (2007).
65. Chase, M.*NIST-JANAF Thermochemical Tables.* 4th ed (American Institute of Physics, 1998).
66. Campbell, C. T., Sprowl, L. H. & Árnadóttir, L. Equilibrium constants and rate constants for adsorbates: two-dimensional (2D) ideal gas, 2D ideal lattice gas, and ideal hindered translator models. *J. Phys. Chem. C* **120**, 10283–10297 (2016).
67. Sprowl, L. H., Campbell, C. T. & Árnadóttir, L. Hindered translator and hindered rotor models for adsorbates: Partition functions and entropies. *J. Phys. Chem. C* **120**, 9719–9731 (2016).
68. Heyd, J., Scuseria, G. E. & Ernzerhof, M. Hybrid functionals based on a screened coulomb potential. *J. Chem. Phys.* **118**, 8207–8215 (2003).
69. Alkauskas, A., Broqvist, P. & Pasquarello, A. Defect levels through hybrid density functionals: Insights and applications. *Phys. Status Solidi B-Basic Solid State Phys.* **248**, 775–789 (2011).
70. Komsa, H.-P. & Pasquarello, A. Assessing the accuracy of hybrid functionals in the determination of defect levels: application to the As antisite in GaAs. *Phys. Rev. B* **84**, 075207 (2011).
71. Modine, N., Wright, A. & Lee, S. Bounds on the range of density-functional-theory point-defect levels in semiconductors and insulators. *Comput. Mater. Sci.* **92**, 431–438 (2014).
72. Ajayi, O. A. et al. Approaching the intrinsic photoluminescence linewidth in transition metal dichalcogenide monolayers. *2D Materials* **4**, 031011 (2017).
73. Yu, Y. et al. Engineering substrate interactions for high luminescence efficiency of transition-metal dichalcogenide monolayers. *Adv. Funct. Mater.* **26**, 4733–4739 (2016).
74. Mouri, S., Miyauchi, Y. & Matsuda, K. Tunable photoluminescence of monolayer MoS_2 via chemical doping. *Nano Lett.* **13**, 5944–5948 (2013).
75. Peimyoo, N. et al. Chemically driven tunable light emission of charged and neutral excitons in monolayer WS_2. *ACS Nano* **8**, 11320–11329 (2014).
76. Plechinger, G. et al. Identification of excitons, trions and biexcitons in single-layer WS_2. *Phys. Status Solidi-Rapid Res. Lett.* **9**, 457–461 (2015).
77. Álvarez Moreno, M. et al. Managing the computational chemistry big data problem: The ioChem-BD platform. *J. Chem. Inf. Model.* **55**, 95–103 (2015).

Acknowledgements

M.R.F. and G.C. acknowledge the High-Performance Computing, Big Data, and Quantum Computing Research Centre, established under the Italian

National Recovery and Resilience Plan (PNRR). F.R. acknowledges financial support from "Technologically Scalable 2D Materials and Extended Operando Measurement Methodologies for Advanced Device Fabrication" 2D-EMMA project - funded by European Union - Next Generation EU within the PRIN 2022 program (D.D. 104 - 02/02/2022 Ministero dell'Università e della Ricerca). This manuscript reflects only the authors' views and opinions and the Ministry cannot be considered responsible for them. All authors acknowledge CINECA for the availability of high-performance computing resources under the Iscra initiative.

Author contributions

G.C. conceived the project, and M.R.F. proposed the methodology. M.G.B. performed all calculations and prepared the manuscript draft. All the authors contributed to the analysis of the results and the writing of the final version of the manuscript.

Competing interests

The authors declare no competing interests.

Additional information

Supplementary information The online version contains supplementary material available at https://doi.org/10.1038/s41524-024-01246-1.

Correspondence and requests for materials should be addressed to Michele Giovanni Bianchi.